

Catalyst-Free Growth of Atomically-thin $\text{Bi}_2\text{O}_2\text{Se}$ Nanoribbons for High-performance Electronics and Optoelectronics

Usman Khan,[†] Lei Tang,[†] Baofu Ding,[†] Luo Yuting,[†] Simin Feng,[†] Wenjun Chen,[†] Muhammad Jahangir Khan,[†] Bilu Liu^{*,†}, and Hui-Ming Cheng^{*,†,#}

[†]Shenzhen Geim Graphene Center, Tsinghua-Berkeley Shenzhen Institute & Institute of Materials Research, Tsinghua Shenzhen International Graduate School, Tsinghua University, Shenzhen 518055, P. R. China.

[#]Shenyang National Laboratory for Materials Science, Institute of Metal Research, Chinese Academy of Sciences, Shenyang 110016, P. R. China.

Correspondence should be addressed to bilu.liu@sz.tsinghua.edu.cn (BL), or hmcheng@sz.tsinghua.edu.cn (HMC)

ABSTRACT

One-dimensional (1D) materials have attracted significant research interest due to their unique quantum confinement effects and edge-related properties. Atomically thin 1D nanoribbon is particularly interesting because it is a valuable platform with physical limits of both thickness and width. Here, we develop a catalyst-free growth method and achieves the growth of $\text{Bi}_2\text{O}_2\text{Se}$ nanostructures with tunable dimensionality. Significantly, $\text{Bi}_2\text{O}_2\text{Se}$ nanoribbons with thickness down to 0.65 nm, corresponding to monolayer, are successfully grown for the first time. Electrical and optoelectronic measurements show that $\text{Bi}_2\text{O}_2\text{Se}$ nanoribbons possess decent performance in terms of mobility, on/off ratio, and photoresponsivity, suggesting their promising for devices. This

work not only reports a new method for the growth of atomically thin nanoribbons but also provides a platform to study properties and applications of such nanoribbon materials at thickness limit.

INTRODUCTION

Dimensionality engineering of materials has been an effective strategy to manipulate their electronic, optical, magnetic, and catalytic properties.^[1] One-dimensional (1D) structure is important because of its unique properties including edge states,^[2] quantum confinement,^[3] ferromagnetic feature,^[4] and high integration density for devices.^[5] In the past two decades, researchers have shown extensive interests to study 1D materials like nanoribbon, nanotube, nanowire, and nanobelt. Recently, there is a trend to prepare 1D nanoribbon from monolayer two-dimensional (2D) materials to make atomically thin nanoribbons and to explore their properties at physical limits of both thickness and width. For example, graphene nanoribbon possesses sizeable bandgaps which are sensitive to its width, expanding the use of graphene in digital electronics. Regarding 2D transition metal dichalcogenides, researchers have shown that MoS₂ nanoribbon is more stable than MoS₂ nanocluster and can exhibit intrinsic magnetism under certain edge structures without the introduction of metal doping in nonmagnetic MoS₂.^[2a] In another material example, it is reported that black phosphorus nanoribbons have a different effective mass of charged carriers and bandgaps, making them promising for optoelectronics and valleytronics.^[6] It is clear that modulating the properties of materials is important and dimensionality engineering is an effective strategy.

Among 2D materials, Bi₂O₂Se has been synthesized only recently with exotic properties and emerged as a promising candidate for future electronics and optoelectronics.^[7] The 2D Bi₂O₂Se has been incorporated in applications including field-effect transistors (FETs),^[8] infrared

photodetection,^[9] spintronics,^[10] photothermal therapy and photoacoustic applications.^[11] Similar to other 2D materials, the growth of atomically thin Bi₂O₂Se nanoribbons is highly motivated. However, there is very rare research in growing Bi₂O₂Se nanoribbons. Recently, Tan et. al. developed a bismuth-catalyzed vapor-liquid-solid (VLS) mechanism to grow Bi₂O₂Se nanoribbons and studied their use in FET.^[12] The thickness of the thinnest VLS grown nanoribbon was around 5 nm, corresponding to 8 atomic layers. FETs based on these Bi₂O₂Se nanoribbons revealed a decent current on/off ratio of >10⁶ and a room temperature field-effect mobility of 220 cm²v⁻¹s⁻¹. It is intriguing to explore the growth and properties of monolayer Bi₂O₂Se nanoribbons, which is not reported previously. In addition, catalysts might raise impurities to Bi₂O₂Se nanoribbons during the VLS growth process. The metal contamination may introduce energy levels in the bandgap of semiconductors and, influence their optical and electrical performance.^[13] Therefore, the development of catalyst-free growth method and exploiting properties of Bi₂O₂Se nanoribbons down to one monolayer are essential but remain challenging.

Here, we developed a catalyst-free CVD method for the synthesis of Bi₂O₂Se nanostructures with tunable dimensionality. By controlling the precursor ratio of Bi₂O₃ and Bi₂Se₃ in the furnace, the growth of 2D Bi₂O₂Se quadrilaterals can be precisely controlled and consequently Bi₂O₂Se nanoribbons with thickness down to monolayer are grown. The CVD grown Bi₂O₂Se nanoribbon-based FET exhibited a high current on/off ratio of >10⁷, and high electron mobility of ~262 cm²V⁻¹s⁻¹. Moreover, photodetectors of Bi₂O₂Se nanoribbons show a high photoresponsivity of ~9.2 × 10⁶ AW⁻¹. The successful growth of Bi₂O₂Se nanoribbons with atomically-thin thickness and decent device performance suggest its great potential for electronic and optoelectronic applications.

RESULTS AND DISCUSSION

$\text{Bi}_2\text{O}_2\text{Se}$ nanostructures are grown by CVD on a mica ($\text{KMg}_3\text{AlSi}_3\text{O}_{10}\text{F}_2$) substrate. The growth of $\text{Bi}_2\text{O}_2\text{Se}$ nanostructures on mica is based on electrostatic interaction between K^+ layer of mica and Se^{2-} layer of $\text{Bi}_2\text{O}_2\text{Se}$ as shown in Figure 1a. Combining the electrostatic interaction between mica and $\text{Bi}_2\text{O}_2\text{Se}$ facilitates the lateral growth of nanostructures. Atomically thin growth of 2D $\text{Bi}_2\text{O}_2\text{Se}$ results because of the lower energy barrier. Dual precursors Bi_2O_3 and Bi_2Se_3 were utilized as co-evaporation sources for the CVD growth of $\text{Bi}_2\text{O}_2\text{Se}$. The experimental setup for the growth of $\text{Bi}_2\text{O}_2\text{Se}$ nanostructures is illustrated in Figure 1b. The typical square-shaped optical microscope (OM) image of $\text{Bi}_2\text{O}_2\text{Se}$ is shown in Figure 1c. The 2D $\text{Bi}_2\text{O}_2\text{Se}$ nanoplate has an ultrasmooth large single crystal with domain size in the range of millimeters. Notably, $\text{Bi}_2\text{O}_2\text{Se}$ with a large domain size of ~ 1.5 mm were obtained by precisely controlling the growth parameters including growth time, growth temperature, and gas flow rate. It was observed that the growth temperature and weight ratio of precursors had a strong impact on the morphology of $\text{Bi}_2\text{O}_2\text{Se}$. Therefore, more precise experiments were conducted by tuning the growth temperature concerning the weight ratio of precursor powders to achieve atomically thin $\text{Bi}_2\text{O}_2\text{Se}$ nanostructures. It was predicted that the synthesis of $\text{Bi}_2\text{O}_2\text{Se}$ nanoribbon went through different growth stages and details are given in supplementary information. As shown in Figure 1d, the as-grown flakes have nanoribbon-like-morphology with an average width and length ~ 80 nm and ~ 200 μm , respectively. The high-magnification OM image of $\text{Bi}_2\text{O}_2\text{Se}$ nanoribbons is shown in Figure 1e. It has been observed that the weight ratio of precursors and growth temperature play important roles in achieving nanostructures with multi-dimensionality including square-shaped $\text{Bi}_2\text{O}_2\text{Se}$, rectangular-shaped- $\text{Bi}_2\text{O}_2\text{Se}$, and ribbon-like morphology of $\text{Bi}_2\text{O}_2\text{Se}$ as summarized in Figure 1f. It is worth mentioning that the nanoribbons were prepared without the use of any catalysts.

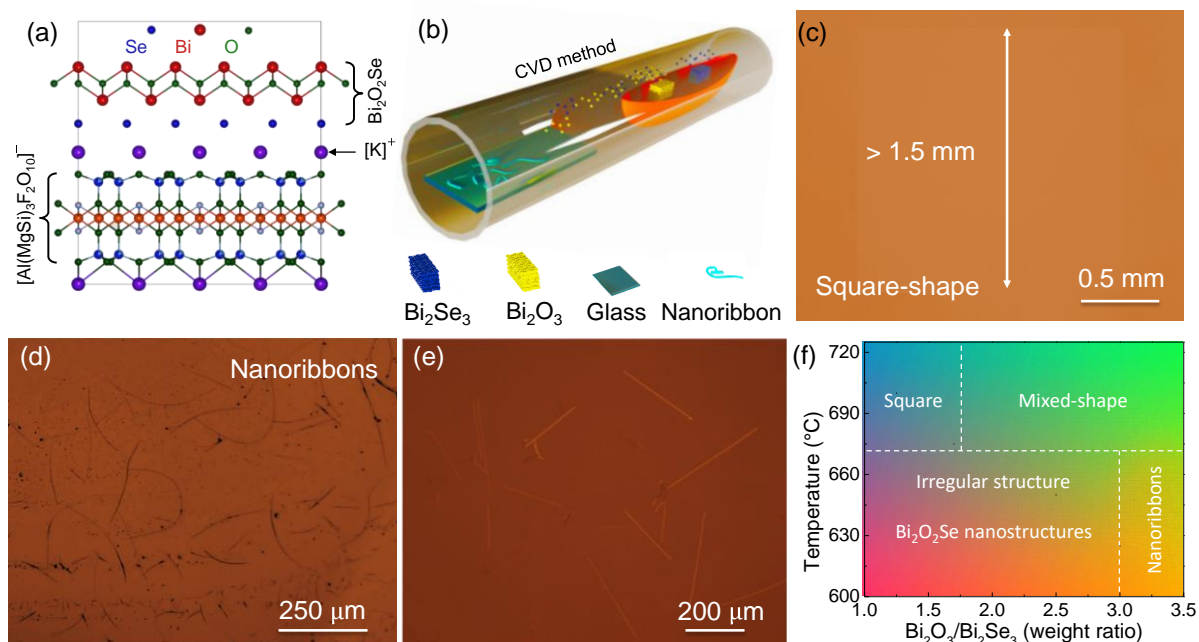


Figure 1: Catalyst-free CVD for the growth of Bi₂O₂Se nanostructures with tunable dimensionality. a) Schematic illustration of the planar growth of Bi₂O₂Se on mica. b) Schematic illustration for CVD growth of Bi₂O₂Se nanostructures with tunable morphology such as 2D quadrilateral Bi₂O₂Se and 1D Bi₂O₂Se nanoribbons whereas dual precursors of Bi₂O₃ and Bi₂Se₃ are used in CVD growth. c) A typical OM image of square-shaped Bi₂O₂Se with an average domain size of > 1.5 mm. OM images of Bi₂O₂Se nanoribbons of (d) low resolution and (e) high-resolution image. f) The schematic design of the morphology control of Bi₂O₂Se nanostructures via tuning temperature and the weight ratio of Bi₂O₃ and Bi₂Se₃ precursors.

Next, we focus on the topography and crystal structure of Bi₂O₂Se nanoribbons. The typical atomic force microscopy (AFM) image of Bi₂O₂Se nanoribbon is displayed in Figure 2a and shows that the topography of the nanoribbon is clean and homogeneous. The thickness of the sample is ~0.65 nm corresponds to the thickness of the monolayer with a width of ~80 nm. Multilayer Bi₂O₂Se nanoribbons have also been synthesized by the CVD method, one sample of which has a

thickness of ~12 nm as shown in Figure 2b. Furthermore, Raman spectroscopy of CVD grown multilayer Bi₂O₂Se nanoribbon is conducted at white circular areas highlighted in the inset of Figure 2c. The point spectra at various positions have analogous characteristic A_{1g} peaks which are centered at ~ 159 cm⁻¹. In addition, Raman mapping of the characteristic peak A_{1g} of nanoribbon depicts similar color contrast across the whole region, indicating the homogeneity of the sample as shown in Figure 2d. Next, we examined the quality of CVD grown samples based on the chemical composition and crystal structure of Bi₂O₂Se nanoribbons. X-ray photoelectron spectroscopy (XPS) confirms the chemical bonding states of Bi, Se and O as shown in Figure 2e-g. The quantitative investigation indicates Bi to Se atomic ratio of 2:1, demonstrating the formation of nanoribbons with adequate stoichiometry. The XPS spectrum of Bi is fitted with two peaks, centered at ~164 and ~159 eV which are corresponding peaks of metallic Bi in bismuth oxide. The fitted peaks of Se 3d_{3/2} and Se 3d_{5/2} are centered at 54 and 53.1 eV. All the identified peaks have their binding energies consistent with the composition of Bi₂O₂Se nanoribbons. This attributes that the excess amount of Bi₂O₃ in synthesized Bi₂O₂Se nanoribbons samples does not affect the elemental composition and reveals consistency with the published work.^[14] Transmission electron microscope (TEM) was employed to further investigate the lattice parameter and crystal structure of Bi₂O₂Se nanoribbons. Figure 2h depicts a typically transferred nanoribbon on Cu grid without any damage. A high-resolution TEM (HRTEM) image of Bi₂O₂Se nanoribbon indicates a d-spacing of 2.7 Å which is accordant with (110) plane of Bi₂O₂Se (Figure 2i).^[14-15] The single crystal behavior of the nanoribbon was further analyzed by a selected area electron diffraction (SAED) image that confirms high crystal quality. The bright spots in the pattern (200), (1 $\bar{1}$ 0), and (110) indicate the tetragonal structure of nanoribbon as shown in Figure 2j. Overall, the analyses

indicate that CVD-grown $\text{Bi}_2\text{O}_2\text{Se}$ nanoribbon has good uniformity, stoichiometry, and high quality.

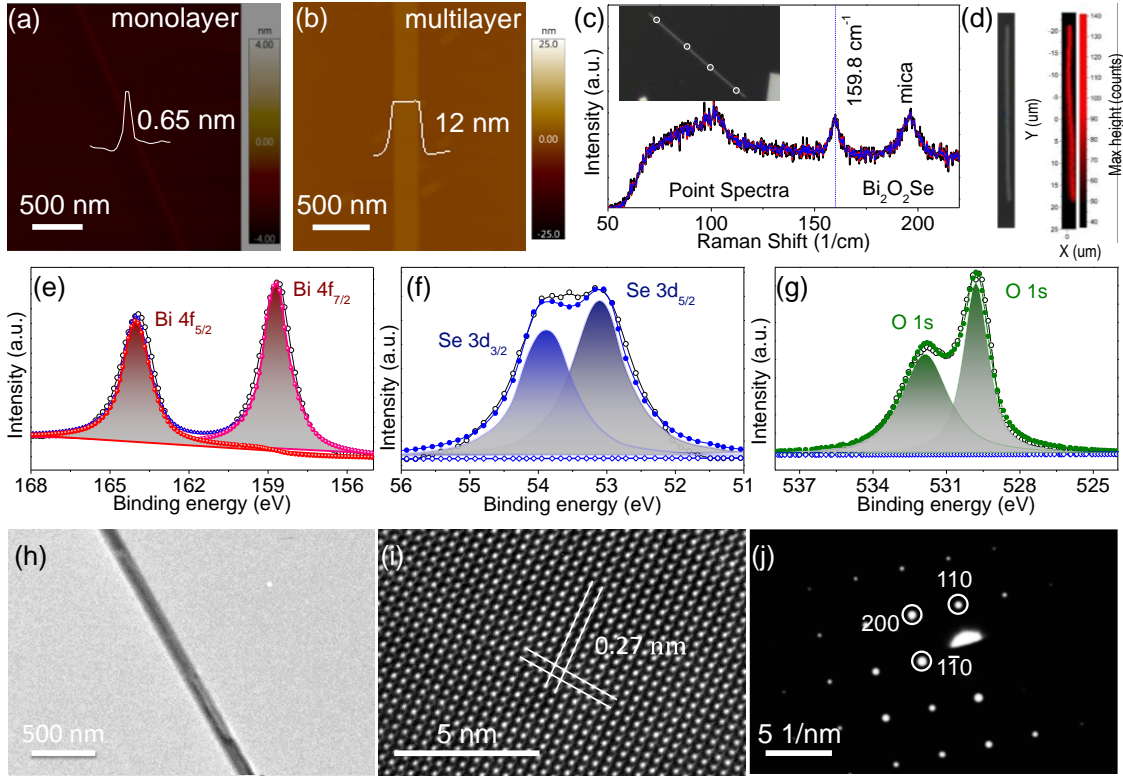


Figure 2: Characterization of monolayer and few-layer $\text{Bi}_2\text{O}_2\text{Se}$ nanoribbons. a) AFM image of a monolayer $\text{Bi}_2\text{O}_2\text{Se}$ nanoribbon with a thickness of ~ 0.65 nm and a width of ~ 80 nm. b) AFM image of a multilayer $\text{Bi}_2\text{O}_2\text{Se}$ nanoribbon with a thickness of ~ 12 nm. c) Point spectra of $\text{Bi}_2\text{O}_2\text{Se}$ nanoribbon collected at different points indicating by white circles in the inset. d) Raman mapping of the nanoribbon recorded at A_{1g} vibrational mode. e-g) XPS spectra of the few-layer $\text{Bi}_2\text{O}_2\text{Se}$ nanoribbons. h) TEM image of $\text{Bi}_2\text{O}_2\text{Se}$ nanoribbon. i) HRTEM image of nanoribbon indicating lattice spacing of 0.27 nm for (110) plane. j) A SAED pattern of $\text{Bi}_2\text{O}_2\text{Se}$ nanoribbon representing its single crystalline feature.

Previous studies have shown that atomically thin 2D $\text{Bi}_2\text{O}_2\text{Se}$ nanoflakes represent high electronic response which further motivates the fabrication of FET based on $\text{Bi}_2\text{O}_2\text{Se}$ nanoribbons. Therefore, considering the importance of $\text{Bi}_2\text{O}_2\text{Se}$ nanoribbons for electronic and optoelectronic applications, samples were initially transferred on SiO_2/Si substrate. To investigate the electrical

performance of Bi₂O₂Se nanoribbons, the transport measurements were investigated with a back-gated FET configuration to determine the feature of thick nanoribbon (12 nm) and studied the contact behavior among nanoribbon and electrodes. The schematic illustration of Bi₂O₂Se nanoribbon-based FET is shown in Figure 3a. The OM image of nanoribbon-based Bi₂O₂Se FET with channel width (W) of ~ 780 nm and length (L) of ~ 2.1 μm is shown in the inset of Figure 3b. Output characteristic curves (I_D - V_D) of the device measured at room temperature are represented in Figure 3b. The back-gate voltage (V_G) has been tuned from -30 V to 30 V with a step voltage of 10 V. It can be observed that drain current (I_D) is highly dependent on V_G which suggests desired gate controllability of the device. The non-linear nature of I_D - V_D curves describes the existence of Schottky junction with a slight difference in barrier height among Bi₂O₂Se nanoribbon and metallic electrodes at both ends of the nanoribbon. The I_D - V_D curves of nanoribbon FET show n-type semiconducting behavior in which I_D increases (decreases) with a raise in positive (negative) V_G . The current ratio amongst V_G of -30 V and 30 V is $\sim 10^7$, which is depicted from the semi-log scale drawn in Figure 3c. The room temperature transfer characteristic curves (I_D - V_G) at different V_D are shown in Figure 3d. The I_D - V_G curves delve the increase in I_D with V_G which further approves n-type conductivity of nanoribbons. The calculated field-effect carrier mobility is ~ 262 $\text{cm}^2\text{V}^{-1}\text{s}^{-1}$ and the corresponding carrier density of Bi₂O₂Se nanoribbon FET is 3.2×10^{12} cm^{-2} at which $V_D = 5\text{V}$. The threshold voltage is determined to be about -21 V by extrapolation of I_D - V_G curves in the linear region. Figure 3e depicts I_D - V_G curves in linear scale at different V_D representing the n-type feature of FET device. The feature is more prominent in the logarithmic scale of I_D - V_G curves (Figure 3f). Table 1 benchmarks the typical research on nanoribbon designed by various synthesis techniques, materials, and electrical performance. We summarized some well-known research on nanoribbon-based FET such as n-type TMDCs, including MoS₂,^[16] CdSe,^[17] tri-chalcogenides

TiS₃,^[18] p-type graphene nanoribbon,^[19] superlattices of AlGaN/GaN,^[20] and III–V compound like boron nitride.^[21] The FET based on Bi₂O₂Se nanoribbons not only achieves high field-effect mobility in comparison with graphene nanoribbon but also simplifies the assembly complexity required for the opening of graphene bandgap. Overall, these experimental results show that Bi₂O₂Se nanoribbon has a high-quality feature and is a promising candidate for high-performance electronics.

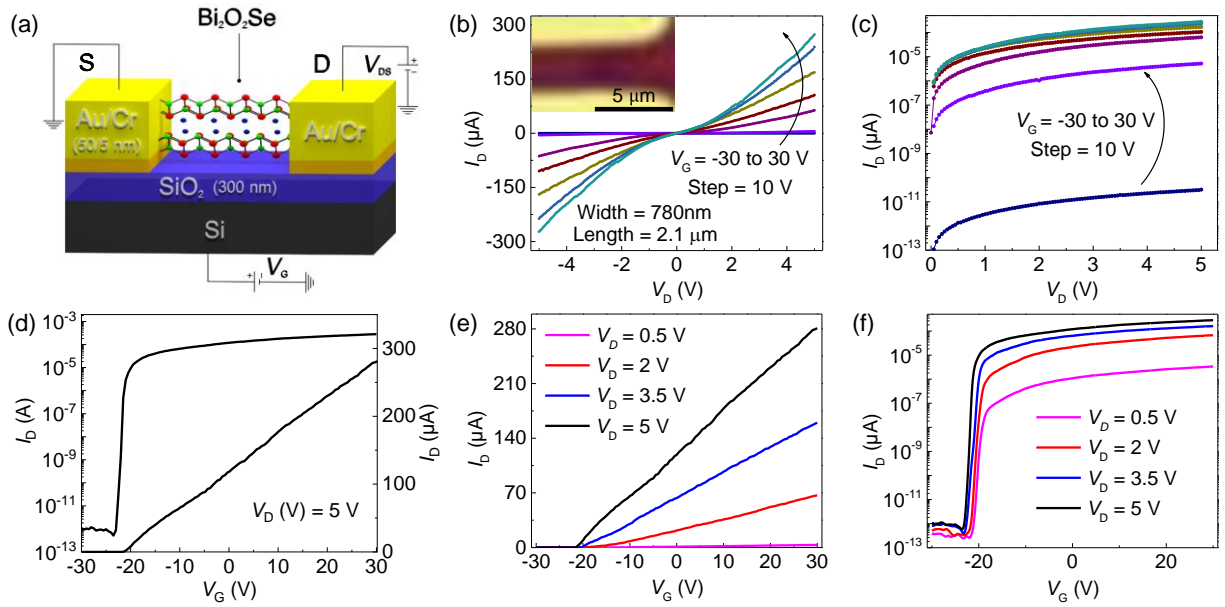


Figure 3: Electrical performance of 1D Bi₂O₂Se nanoribbon. a) Schematic illustration of back-gated Bi₂O₂Se nanoribbon-based FET. b) The inset depicts OM of Bi₂O₂Se nanoribbon-based FET device with a channel length (L) and width (W) of 2.1 μm and 780 nm, respectively, whereas the main figure indicates output characteristic curves (I_D - V_D) of the device as a function of gate voltage (V_G) in linear scale (b) and logarithmic scale (c). d) The transfer characteristic curves (I_D - V_G) at V_D of 5V. e-f) I_D - V_G family curves of the device as a function of V_D are represented in linear and logarithmic scales.

Table 1. Performance comparison of nanoribbon field-effect transistors reported in the literature.

Materials	Method	Nature (-type)	FET architecture	On/off ratio	Mobility (cm ² /Vs)	Reference
Black phosphorus	Plasma etching	p	Top-gate	10 ³	310	[22]
Graphene	Unzip MWCNTs	p	Back-gate	-	1500	[19a]
Graphene	Bottom-up approach	p	Back-gate	10 ⁶	200	[19b]
hBN	MWBNNTs	n	-	-	58.8	[21]
AlGaIn/GaN	Plasma etching	n	Top-gate	-	289	[20]
TiS ₃	Heat treatment	n	Back-gate	10 ⁴	2.6	[18]
CdSe	Thermal Evaporation	n	Back-gate	10 ⁴	9.6	[17]
MoS ₂	Plasma etching	n	Back-gate	10 ⁷	21.8	[16]
Bi ₂ O ₂ Se	VLS	n	Top-gate	10 ⁶	220	[12]
Bi ₂ O ₂ Se	CVD	n	Back-gate	>10 ⁷	~262	This work

Notes. MWCNTs=Multiwall carbon nanotubes, MWBNNTs=Multiwall boron nitride nanotubes.

Generally, few-layer semiconductors with suitable bandgaps are promising materials for photodetectors because of low energy loss during charge recombination, enhanced light absorption and better drain to source charge transfer.^[23] Considering the advantage of the suitable bandgap of Bi₂O₂Se, we characterized the performance of photodetector based on Bi₂O₂Se nanoribbon and is illustrated in Figure 4a. Figure 4b reveals zero-gated I_D - V_D curves in dark and under light illumination. The I_D of the device on a linear scale at different power densities is represented in the inset of Figure 4b. The device exhibits dark current (I_D) of ~100 μ A at $V_D = \pm 5$ V. The maximum photocurrent ($I_{ph} = I_{light} - I_{dark}$) generated at $V_D = 5$ V ($V_G = 0$ V) is 130 μ A under power density of 66.84 W/m². The photocurrent (I_{ph}) increases under illumination because of increased photogenerated charge density. The low power of laser light would possibly excite the electron-hole pairs in the nanoribbon. These pairs diffuse to the depletion region, where the built-in electric field is strong enough to dissociate these pairs into the free electrons and holes. The collection of these free charges by electrodes finally results in the linear increase of photocurrent. Under strong light intensity, the newly charge-balanced state stimulates incoming charge carriers at Schottky junction and depletion region squeezes. The depletion width is consequently reduced, thereby decreasing the strength of the electric field and the resultant dissociation efficiency of electron-

hole pairs. This hinders the further increase of photoresponse,^[24] as presented by the saturation behavior of photocurrent $\sim 66.84 \text{ W/m}^2$ in Figure 4b. The trend of I_{ph} as a function of different light intensities follows the power-law $I_{\text{ph}} \propto P^\gamma$ where γ represents I_{ph} response on light and is shown in Figure 4c. The values of the exponential function γ have been derived by a non-linear curve fitting and it yields $\gamma = 0.55, 0.5, 0.44,$ and 0.39 for V_{D} of 5, 4, 3, and 2 V, respectively. The non-unity of γ suggests complex mechanisms that would involve charge trapping, electron-hole pair generation and recombination in $\text{Bi}_2\text{O}_2\text{Se}$ nanoribbons.^[25] The time-resolved photoresponse of $\text{Bi}_2\text{O}_2\text{Se}$ nanoribbon-based photodetector is measured by periodically switching of 590 nm laser light with a light intensity of 66.84 W/m^2 at $V_{\text{D}}=5 \text{ V}$ (Figure 4d). It can be depicted that I_{D} increases abruptly and becomes stabilized at $\approx 230 \mu\text{A}$, followed by dropping down to initial $I_{\text{D}} \approx 100 \mu\text{A}$ after removal of light. The device responded excellent on and off swapping of voltage with good stability and reproducibility which depicts excellent reproducibility of photodetector. The rise (τ_{rise}) and decay (τ_{decay}) time constants of the device are obtained with normalized temporal photoresponse as shown in Figure 4e. By defining τ_{rise} (τ_{decay}) as the time required by the photodetector to increase (decrease) photocurrent from 10% I_{D} to 90% I_{D} (90% I_{D} to 10% I_{D}), it is characterized to be $\sim 39 \text{ ms}$ (63 ms).

The other figure of merits of the photodetectors are responsivity (R) and detectivity (D^*) and are represented in Figure 4f. The maximum spectral R of the $\text{Bi}_2\text{O}_2\text{Se}$ photodetector has been measured to be $9.19 \times 10^6 \text{ AW}^{-1}$ at zero-gate voltage. The high value of R is because of a strong induced electric field at $\text{Bi}_2\text{O}_2\text{Se}$ nanoribbon and metal contact Schottky junction. The corresponding value of specific detectivity at zero-gate voltage is $2.08 \times 10^{12} \text{ Jones}$. The outstanding performance of the device is because of the facts: (i) single-crystalline nature of nanoribbons that suppresses scattering centers and attributes more efficient carriers at contact

region and (ii) absence of contamination that can deteriorate the carrier traps and reduce the non-radiative recombination centers in nanoribbons. The R as a function of light intensity is shown in Figure 4f. It is observed that the R decreases as the light intensity rises which can be elucidated as follows: three different mechanisms occur due to the irradiation of light on semiconducting nanoribbons, namely electron and hole pair generation, electron and hole pair recombination and transport of photogenerated charges due to a strong induced electric field.^[25b, 26] The photogenerated charge carriers are proportional to the intensity of incident light. The strong induced field suppresses the recombination at low intensity and generates high R . Overall, these experimental results together with tunable dimensional growth of $\text{Bi}_2\text{O}_2\text{Se}$ depict that $\text{Bi}_2\text{O}_2\text{Se}$ nanoribbon is a promising candidate for high-performance optoelectronics.

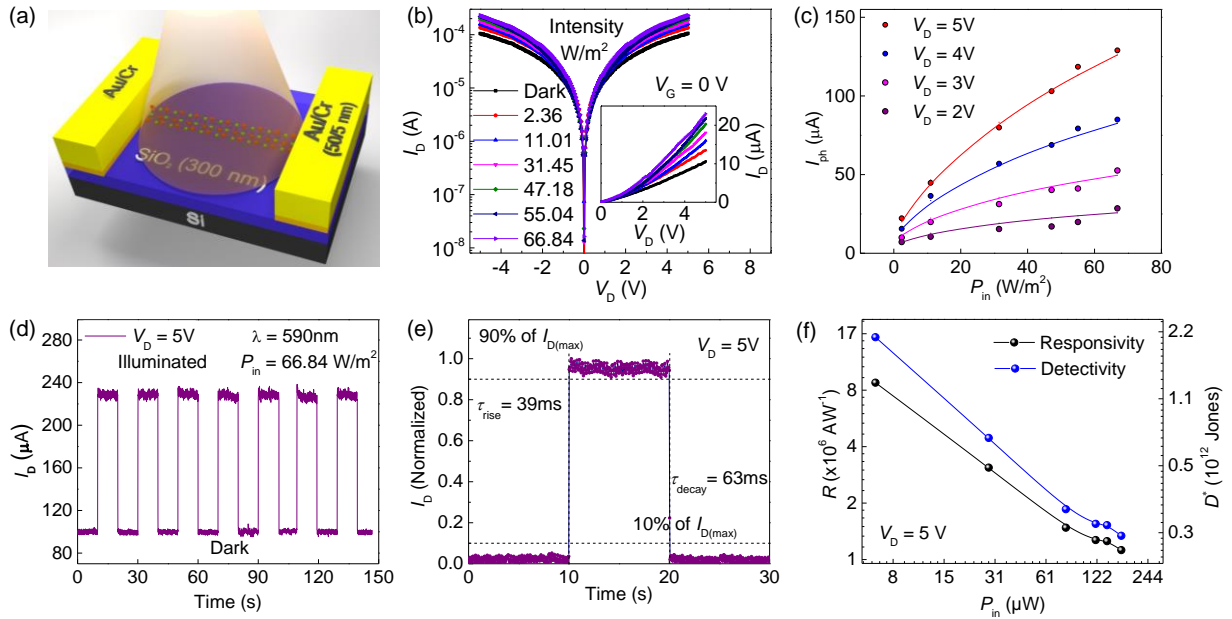


Figure 4: Optoelectronic performance of 1D $\text{Bi}_2\text{O}_2\text{Se}$ nanoribbon. a) The output characteristic curves (I_D - V_D) of zero-gated $\text{Bi}_2\text{O}_2\text{Se}$ nanoribbon photodetector under light illumination of 590 nm at different intensities; the linear scale of curves is shown in the inset. b) The photocurrent variation with light intensity at zero-gate bias for different drain voltages follows the power law. c) The on to off photocurrent to dark current ratio for various light intensities at zero-gate voltage.

d) The on/off current switching of Bi₂O₂Se nanoribbon photodetector for laser intensity of 66.84 W/m² depicts repeatability and stability of the device. e) Time-resolved photoresponse of the photodetector reveals the rise and decay times of 39 and 63 ms, respectively. f) Variation of spectral responsivity and specific detectivity of the device as a function of incident power drain voltage.

CONCLUSION

We have developed a catalyst-free CVD method to grow Bi₂O₂Se with tunable dimensionality ranging from 2D quadrilateral shape to 1D nanoribbons on a mica substrate. The morphology of nanostructures was controlled by tuning the growth conditions and mechanisms. Monolayer Bi₂O₂Se nanoribbons with a thickness of 0.65 nm were grown for the first time. The FETs made of Bi₂O₂Se nanoribbons exhibited n-type semiconductor characteristics with high electron mobility of $\sim 262 \text{ cm}^2\text{V}^{-1}\text{s}^{-1}$ and a high on/off ratio of $>10^7$. In addition, Bi₂O₂Se nanoribbon-based photodetector exhibits decent photoresponsivity of $\sim 9.2 \times 10^6 \text{ AW}^{-1}$. Considering their high quality, good uniformity and stoichiometry, our results suggest the potential of these monolayer thick nanoribbons for a wide range of applications.

AUTHOR INFORMATION

Corresponding Author

*E-mail: bilu.liu@sz.tsinghua.edu.cn, hmcheng@sz.tsinghua.edu.cn

Notes

The authors declare no competing financial interest.

ACKNOWLEDGMENTS

We acknowledge support by the National Natural Science Foundation of China (Nos. 51991340, 51920105002, 51991343, and 51950410577), Guangdong Innovative and Entrepreneurial Research Team Program (No. 2017ZT07C341), the Bureau of Industry and Information Technology of Shenzhen for the “2017 Graphene Manufacturing Innovation Center Project” (No. 201901171523), and the Shenzhen Basic Research Project (Nos. JCYJ20200109144620815, JCYJ20190809180605522 and JCYJ20200109144616617).

REFERENCE

- [1] a) T. Chowdhury, J. Kim, E. C. Sadler, C. Li, S. W. Lee, K. Jo, W. Xu, D. H. Gracias, N. V. Drichko, D. Jariwala, T. H. Brintlinger, T. Mueller, H.-G. Park, T. J. Kempa, *Nature Nanotechnology* **2020**, 15, 29; b) S. Li, Y.-C. Lin, W. Zhao, J. Wu, Z. Wang, Z. Hu, Y. Shen, D.-M. Tang, J. Wang, Q. Zhang, H. Zhu, L. Chu, W. Zhao, C. Liu, Z. Sun, T. Taniguchi, M. Osada, W. Chen, Q.-H. Xu, A. T. S. Wee, K. Suenaga, F. Ding, G. Eda, *Nature Materials* **2018**, 17, 535; c) A. Aljarb, J.-H. Fu, C.-C. Hsu, C.-P. Chuu, Y. Wan, M. Hakami, D. R. Naphade, E. Yengel, C.-J. Lee, S. Brems, T.-A. Chen, M.-Y. Li, S.-H. Bae, W.-T. Hsu, Z. Cao, R. Albaridy, S. Lopatin, W.-H. Chang, T. D. Anthopoulos, J. Kim, L.-J. Li, V. Tung, *Nature Materials* **2020**, 19, 1300; d) C. Zhang, Y. Luo, J. Tan, Q. Yu, F. Yang, Z. Zhang, L. Yang, H.-M. Cheng, B. Liu, *Nature Communications* **2020**, 11, 3724.
- [2] a) Y. Li, Z. Zhou, S. Zhang, Z. Chen, *Journal of the American Chemical Society* **2008**, 130, 16739; b) H. Xu, S. Liu, Z. Ding, S. J. R. Tan, K. M. Yam, Y. Bao, C. T. Nai, M.-F. Ng, J. Lu, C. Zhang, K. P. Loh, *Nature Communications* **2016**, 7, 12904.
- [3] G. Liang, N. Neophytou, D. E. Nikonov, M. S. Lundstrom, *IEEE Transactions on Electron Devices* **2007**, 54, 677.
- [4] G. Xu, X. Wang, Y. Sun, X. Chen, J. Zheng, L. Sun, L. Jiao, J. Li, *Nano Research* **2015**, 8, 2946.
- [5] Z. Chen, A. Narita, K. Müllen, *Advanced Materials* **2020**, 32, 2001893.
- [6] a) V. Tran, L. Yang, *Physical Review B* **2014**, 89, 245407; b) X. Han, H. M. Stewart, S. A. Shevlin, C. R. A. Catlow, Z. X. Guo, *Nano Letters* **2014**, 14, 4607; c) Z. Liu, Y. Sun, H. Cao, D. Xie, W. Li, J. Wang, A. K. Cheetham, *Nature Communications* **2020**, 11, 3917; d) M. Liu, S. Feng, Y. Hou, S. Zhao, L. Tang, J. Liu, F. Wang, B. Liu, *Materials Today* **2020**, 36, 91.
- [7] a) Q. Wei, C. Lin, Y. Li, X. Zhang, Q. Zhang, Q. Shen, Y. Cheng, W. Huang, *Journal of Applied Physics* **2018**, 124, 055701; b) T. Cheng, C. Tan, S. Zhang, T. Tu, H. Peng, Z. Liu, *The Journal of Physical Chemistry C* **2018**, 122, 19970; c) M. Wu, X. C. Zeng, *Nano Letters* **2017**, 17, 6309; d) W. Chen, U. Khan, S. Feng, B. Ding, X. Xu, B. Liu, *Advanced Functional Materials* **2020**, 30, 2004960.
- [8] U. Khan, Y. Luo, L. Tang, C. Teng, J. Liu, B. Liu, H.-M. Cheng, *Advanced Functional Materials* **2019**, 29, 1807979.
- [9] J. Yin, Z. Tan, H. Hong, J. Wu, H. Yuan, Y. Liu, C. Chen, C. Tan, F. Yao, T. Li, Y. Chen, Z. Liu, K. Liu, H. Peng, *Nature Communications* **2018**, 9, 3311.
- [10] R. Quhe, J. Liu, J. Wu, J. Yang, Y. Wang, Q. Li, T. Li, Y. Guo, J. Yang, H. Peng, M. Lei, J. Lu, *Nanoscale* **2019**, 11, 532.
- [11] J. Yang, R. Quhe, Q. Li, S. Liu, L. Xu, Y. Pan, H. Zhang, X. Zhang, J. Li, J. Yan, B. Shi, H. Pang, L. Xu, Z. Zhang, J. Lu, J. Yang, *Advanced Electronic Materials* **2019**, 5, 1800720.

- [12] M. Y. Congwei Tan, Shipu Xu, Jinxiong Wu, Shulin Chen, Yan Zhao, Cong Liu, Yichi Zhang, Teng Tu, Tianran Li, Peng Gao, Hailin Peng, *Acta Physico-Chimica Sinica* **2020**, 36, 1908038.
- [13] a) O. Moutanabbir, D. Isheim, H. Blumtritt, S. Senz, E. Pippel, D. N. Seidman, *Nature* **2013**, 496, 78; b) J. E. Allen, E. R. Hemesath, D. E. Perea, J. L. Lensch-Falk, Z. Y. Li, F. Yin, M. H. Gass, P. Wang, A. L. Bleloch, R. E. Palmer, L. J. Lauhon, *Nature Nanotechnology* **2008**, 3, 168; c) S. Francoeur, S. Tixier, E. Young, T. Tiedje, A. Mascarenhas, *Physical Review B* **2008**, 77, 085209; d) J. Zhu, H. Peng, C. K. Chan, K. Jarausch, X. F. Zhang, Y. Cui, *Nano Letters* **2007**, 7, 1095.
- [14] J. Wu, C. Tan, Z. Tan, Y. Liu, J. Yin, W. Dang, M. Wang, H. Peng, *Nano Letters* **2017**, 17, 3021.
- [15] J. Wu, H. Yuan, M. Meng, C. Chen, Y. Sun, Z. Chen, W. Dang, C. Tan, Y. Liu, J. Yin, Y. Zhou, S. Huang, H. Q. Xu, Y. Cui, H. Y. Hwang, Z. Liu, Y. Chen, B. Yan, H. Peng, *Nature Nanotechnology* **2017**, 12, 530.
- [16] H. Liu, J. Gu, P. D. Ye, *IEEE Electron Device Letters* **2012**, 33, 1273.
- [17] J. S. Jie, W. J. Zhang, Y. Jiang, S. T. Lee, *Applied Physics Letters* **2006**, 89, 133118.
- [18] J. O. Island, M. Buscema, M. Barawi, J. M. Clamagirand, J. R. Ares, C. Sánchez, I. J. Ferrer, G. A. Steele, H. S. J. van der Zant, A. Castellanos-Gomez, *Advanced Optical Materials* **2014**, 2, 641.
- [19] a) L. Jiao, X. Wang, G. Diankov, H. Wang, H. Dai, *Nat Nanotechnol* **2010**, 5, 321; b) X. Wang, Y. Ouyang, X. Li, H. Wang, J. Guo, H. Dai, *Physical Review Letters* **2008**, 100, 206803.
- [20] S. Joglekar, M. Azize, E. J. Jones, D. Piedra, S. Gradečak, T. Palacios, *IEEE Transactions on Electron Devices* **2016**, 63, 318.
- [21] H. Zeng, C. Zhi, Z. Zhang, X. Wei, X. Wang, W. Guo, Y. Bando, D. Golberg, *Nano Letters* **2010**, 10, 5049.
- [22] X. Feng, X. Huang, L. Chen, W. C. Tan, L. Wang, K.-W. Ang, *Advanced Functional Materials* **2018**, 28, 1801524.
- [23] D. Lembke, S. Bertolazzi, A. Kis, *Accounts of Chemical Research* **2015**, 48, 100.
- [24] a) J. Miao, W. Hu, N. Guo, Z. Lu, X. Zou, L. Liao, S. Shi, P. Chen, Z. Fan, J. C. Ho, T.-X. Li, X. S. Chen, W. Lu, *ACS Nano* **2014**, 8, 3628; b) Y. Hu, Y. Chang, P. Fei, R. L. Snyder, Z. L. Wang, *ACS Nano* **2010**, 4, 1234.
- [25] a) C.-H. Kuo, J.-M. Wu, S.-J. Lin, W.-C. Chang, *Nanoscale Research Letters* **2013**, 8, 327; b) X. Xie, S.-Y. Kwok, Z. Lu, Y. Liu, Y. Cao, L. Luo, J. A. Zapien, I. Bello, C.-S. Lee, S.-T. Lee, W. Zhang, *Nanoscale* **2012**, 4, 2914.
- [26] a) D. Zheng, J. Wang, W. Hu, L. Liao, H. Fang, N. Guo, P. Wang, F. Gong, X. Wang, Z. Fan, X. Wu, X. Meng, X. Chen, W. Lu, *Nano Letters* **2016**, 16, 2548; b) E. Liu, M. Long, J. Zeng, W. Luo, Y. Wang, Y. Pan, W. Zhou, B. Wang, W. Hu, Z. Ni, Y. You, X. Zhang, S. Qin, K. W. Yi Shi, T. Taniguchi, H. Yuan, H. Y. Hwang, Y. Cui, F. Miao, D. Xing, *Advanced Functional Materials* **2016**, 26, 1938.